mathematics

MDPI

Article

A Method for Predicting the Timing of Mine Earthquakes Based on Deformation Localization States

Chenli Zhu [1], Linlin Ding [2,*], Yimin Song [3] and Yuda Li [2]

[1] College of the Environment, Liaoning University, Shenyang 110036, China; 4022210198@smail.lnu.edu.cn
[2] College of the Information, Liaoning University, Shenyang 110036, China; 4032242440@smail.lnu.edu.cn
[3] School of Civil Engineering, North China University of Technology, Beijing 100144, China; songyimin@ncut.edu.cn
* Correspondence: dinglinlin@lnu.edu.cn

Abstract: As a prevalent geological hazard in underground engineering, the accurate prediction of mine earthquakes is crucial for ensuring operational safety and enhancing mining efficiency. The deformation localization method effectively predicts the instability of disaster rocks, yet the timing of mine earthquakes remains understudied. This study established a correlation between rock deformation localization and seismic activity within mines through theoretical derivations. A predictive model algorithm for forecasting mine earthquake timing was developed based on Saito's theory, integrating optics, acoustics, and mathematical modeling theories. The "quiet period" was identified as a significant precursor; thus, the model used the initiation of deformation localization to accurately predict rock failure. Using the model, a coal mine in Inner Mongolia was selected as a case study to predict a historical mining earthquake. The results indicated that the following: (1) Deformation localization and the "quiet period" of microseismic (MS) and acoustic emission (AE) activities were identified as two key pre-cursory indicators. The model utilized the initiation time of deformation localization and the inflection point of the "quiet period" in MS and AE activity as primary parameters. (2) For predicting rock failure times, the earliest prediction time deviates from the actual failure time by 143 s. The accuracy rate of predicted time points falling within a 90% confidence interval of the actual failure times is 100%. The model achieved 60% in forecasting the occurrence times of mine earthquakes. (3) The model's prediction accuracy improved as the starting time parameter more closely approximated the actual initiation time of deformation localization, with the accuracy increasing from 0% to 100%.

Keywords: mine earthquakes; time prediction model; deformation localization; acoustic emission; microseismic

MSC: 86-08

check for updates

Academic Editors: Jie Wen, Cai Xu and Jinrong Cui

Received: 21 November 2024
Revised: 17 December 2024
Accepted: 23 December 2024
Published: 26 December 2024

Citation: Zhu, C.; Ding, L.; Song, Y.; Li, Y. A Method for Predicting the Timing of Mine Earthquakes Based on Deformation Localization States. *Mathematics* **2025**, *13*, 40. https://doi.org/10.3390/math13010040

Copyright: © 2024 by the authors. Licensee MDPI, Basel, Switzerland. This article is an open access article distributed under the terms and conditions of the Creative Commons Attribution (CC BY) license (https://creativecommons.org/licenses/by/4.0/).

1. Introduction

Mine earthquakes are a complex dynamic phenomenon that occurs when stress conditions within the overlying rock are altered by mining activities, leading to the release of stored elastic energy [1,2]. These earthquakes predominantly occur in the goaf of adjacent workings. The ground experiences noticeable tremors, but there is no tunnel damage, no equipment damage, and no casualties underground. In recent years, as mining depth and intensity have increased, mine earthquakes have become more frequent. As shown in

Figure 1, these shows the regions in China where mining earthquakes have occurred frequently in recent years. Some of these earthquakes not only induce underground coal bursts and coal and gas outbursts, which are secondary disasters, but also result in strong ground tremors, building damage, and other serious consequences [3,4]. This transformation turns mine seismicity from a mining safety issue into a public safety concern [5,6]. Consequently, mine seismic hazard management is garnering increasingly widespread attention.

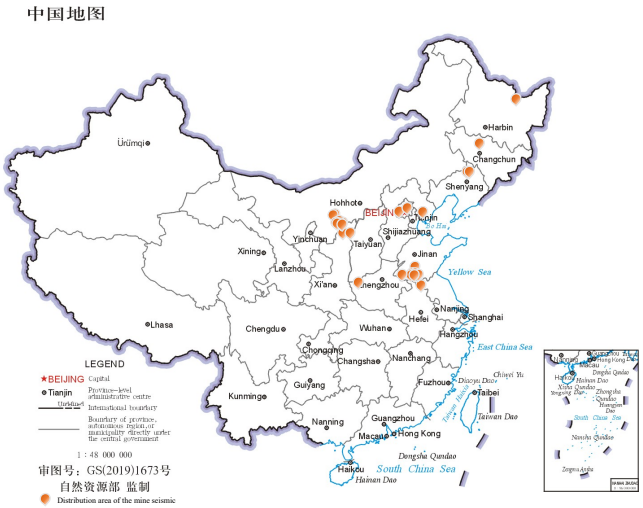


Figure 1. The distribution of typical mine earthquakes in Chinese mining areas.

Deformation localization refers to the phenomenon where certain areas within a rock mass exhibit a deformation behavior that is significantly different from the surrounding areas due to stress concentration [7–10]. This phenomenon is often regarded as a precursor to the imminent occurrence of mine earthquakes. To effectively predict coal-rock catastrophes and mine power disasters, experts and scholars worldwide thoroughly study the deformation localization phenomenon and identify key pre-cursor information that foretells the destabilization and damage of coal-rock. By extracting this characteristic information, a reliable scientific basis is provided for the prediction and early warning of coal-rock catastrophes and mine power disasters. Hao et al. [11,12] found that deformation localization precedes rock rupture by monitoring strain evolution in uniaxial compression to predict rupture timing. Xue et al. [13] used DIC to measure rock surface displacement and strain by estimating rupture time from the localized zone's response function's power–law relationship, providing a practical rupture prediction method. These methods track rock mass surface strain, but underground, such data is hard to obtain. Researchers instead monitor internal rock rupture's physical signals, linking them to deformation characteristics to assess rock instability in real engineering contexts. Among these methods, MS (AE) monitoring [14–18] stands out as a widely used technique in the field of underground engineering. The reason for its widespread adoption is that MS (AE) activity can reflect changes in the stress state of the underground rock mass. Consequently, disaster prediction can be achieved by establishing a link between MS (AE) activity and localization characteristics. Feng et al. [19] found that micro-rupture AE events near plastic stress drops indicate strong localization, constructing a coal burst hazard index. Pan et al. [20] showed that MS event indicators reflect deformation localization, predicting coal burst areas. Jia et al. [21] linked MS events to rock failure and stress concentration while assessing goaf stability. Wang et al. [22] combined deformation localization with MS event distribution to identify hazardous areas, using Bayesian networks to improve coal burst risk prediction. Lai et al. [23] modeled rock bursts from localized deformation in deep coal mines, finding that the "sandwiched rock pillar-B6 roof" structure causes rock bursts with increasing

mining depth. Deformation localization is a major sign of rock failure. MS data from engineering sites further reveal these localization features, offering a new perspective on the study of coal mine disasters that are primarily caused by rock failure. Certainly, with the advancement of artificial intelligence technology [24–29] and the extensive application of neural network models [30,31], significant progress has been made in predicting mine power disasters. For instance, Ma et al. [32] devised a LightGBM-TCN-RF model to forecast rock burst risk levels in mines. Their research demonstrated that this model markedly surpassed alternative models like KNN and SVM. In another study, Ma et al. [33] utilized 289 days of microseismic monitoring data from the Qinling water conveyance tunnel to construct rock burst prediction models. They found the Borderline-SMOTE1-Adaboost model to be highly effective, accurately predicting all ten severe rock bursts during the test phase, thus indicating its potential for early warnings in deep-buried tunnel construction. Basnet et al. [34] explored the viability of parametric models for predicting short-term rock burst severity using microseismic data. They applied logistic regression and support vector machine models to both normally and non-normally distributed datasets. The findings revealed that the parametric model performed better in assessing short-term rock burst risks, particularly when data availability was limited. Sun et al. [35] introduced an optimal feature selection and Bayesian hidden layer weighted probability stacking model (OFS-Bayes-WPS) for predicting short-term rock burst intensity using microseismic data. This model excelled over other single and ensemble models and exhibited remarkable performance in predicting new rock burst cases across various locations. However, the prevailing machine learning-centric approaches predominantly harness extensive datasets from real-time site observations for training. A recurring shortfall lies in their inadequacy to encompass the intricate physical attributes inherent to underground engineering, thereby compromising model interpretability. Furthermore, there exists an unmet need for predictive models based on rock deformation localization phenomena. Existing theoretical constructs, constrained by reliance on solitary metrics, grapple with merging experimental findings in live monitoring contexts, impeding the precise prediction of mine earthquakes.

The research introduces a method for predicting the timing of mine earthquakes using rock deformation localization. It establishes a theoretical link between mine earthquakes and rock deformation localization and develops a time prediction model based on Saito's theory. This method can predict rock failure and the timing of mine earthquakes, providing a new theoretical framework for rock failure prediction and a scientific basis for the early warning and prevention of mine earthquakes.

2. Deformation Localization and Mine Earthquakes Correlation

Mine earthquakes represent the response of rock mass to the deformation and rupture of underground structures. By establishing the correspondence between mine earthquakes and the conditions under which rock deformation localization occurs, we can provide a theoretical basis for predicting mine earthquakes and offer guidance in this area [20,36].

(1) Conditions of the occurrence of mine earthquakes

Under the influence of surface force P and mass force F, the rock deformation system results in displacement u, stress σ, and strain ε. The volumes of the plastic softening zone and the remaining elastic zone are vs. and V_e, respectively. At a certain equilibrium state, a small virtual displacement Δu is imposed on the rock, resulting in virtual stress $\Delta\sigma$ and virtual strain $\Delta\varepsilon$. If the virtual work performed by the external forces exceeds the increase

in internal strain energy, the rock deformation system becomes unstable, which is the condition for the occurrence of a mine earthquake:

$$\int_{V_e+V_s} F^T \Delta u dv + \int_{\Gamma} P^T \Delta u ds \geq \int_{V_e} (\sigma + \Delta\sigma)\Delta\varepsilon dv + \int_{V_s} (\sigma + \Delta\sigma)\Delta\varepsilon dv \quad (1)$$

As the rock system is in equilibrium, it adheres to the virtual work equation, which states that the virtual work performed by the external forces during virtual displacement is equal to the virtual work performed by the stresses during virtual strain. This principle can be expressed as follows:

$$\int_{V_e+V_s} F^T \Delta u dv + \int_{\Gamma} P^T \Delta u ds = \int_{V_e} \sigma^T \Delta\varepsilon dv + \int_{V_s} \sigma^T \Delta\varepsilon dv \quad (2)$$

Simplified by Equations (1) and (2), the conditions for coal bursts to occur can be determined as follows:

$$\int_{V_e} \sigma^T \Delta\varepsilon dv + \int_{V_s} \sigma^T \Delta\varepsilon dv \leq 0 \quad (3)$$

(2) Conditions for the occurrence of deformation localization of the rock

The rock deformation system experiences stress σ and strain ε under the application of surface force P. A portion of the area becomes a deformation-softened region when stress concentrations exceed the peak strength. This softened region is denoted as V_s, while the remaining regions maintain elastic deformation zones with volume V_e. Assuming that a disturbance increment ΔP is induced in the surface force loading of the rock system in this state, resulting in stress growth $\Delta\sigma$, strain growth $\Delta\varepsilon$, and displacement growth Δu, then:

$$\int_{V_e+V_s} B^T \Delta\sigma dV = \Delta P \quad (4)$$

where B is the strain matrix.

The relationship between $\Delta\varepsilon$ and Δu is as follows:

$$\Delta\varepsilon = B\Delta u \quad (5)$$

The ontological relationship of the rock in the elastic zone is as follows:

$$\Delta\sigma = D^e \Delta\varepsilon \quad (6)$$

The ontological relationship of the rock in the softening zone is as follows:

$$\Delta\sigma = D^{ep} \Delta\varepsilon \quad (7)$$

where D^e and D^{ep} are the elastic and elastoplastic matrices, respectively.

Substituting Equations (5)–(7) into Equation (4) yields the following:

$$\Delta P = K\Delta U \quad (8)$$

$$K = \int_{V_e} B^T D^e \Delta U B dV + \int_{V_e} B^T D^{ep} B dV \quad (9)$$

where K is the stiffness matrix and ΔU is the total displacement vector.

According to the definition of deformation localization, if under the action of the same increment ΔP, another set of displacement increment distributions different from ΔU exists,

this is the point at which damage localization begins. Let the other set of the displacement distribution generated under the action of ΔP be ΔU^*, then:

$$\Delta P = K\Delta U^* \tag{10}$$

It holds:

$$K\Delta a = 0 \tag{11}$$

where $\Delta a = \Delta U - \Delta U^*$ is the difference between two different displacement field distributions.

If a non-zero solution exists, then two displacement distributions exist, i.e., damage localization begins, and the condition for the existence of a non-zero solution is as follows:

$$detK = 0 \tag{12}$$

$$\{\Delta U\}^T K\Delta U = 0 \tag{13}$$

$$\int_{V_e} \{\Delta\sigma\}^T \Delta\varepsilon dV + \int_{V_s} \{\Delta\sigma\}^T \Delta\varepsilon dV = 0 \tag{14}$$

The initiation of rock failure localization coincides with the critical conditions for mine earthquake occurrence. As the stress on the rock approaches its strength limit, damage localization occurs, leading to a strain concentration area. Within this area, micro-fractures intensify and coalesce, forming macro-fractures. When these macroscopic fissures destabilize and expand, a mine earthquake occurs through the violent release of elastic energy. After the earthquake, the system regains equilibrium, and the expansion of fissures either ceases or decelerates, which stabilizes and terminates the mine earthquake phenomenon. This description outlines the physical process of a mine earthquake in terms of rock failure.

In summary, the deformation and destruction process of a mine earthquake is essentially the localization of deformation and rupture within the rock. In other words, deformation localization in rock can be considered a precursor to a mine earthquake.

3. Time Prediction Methods

3.1. Calculation Principle for the Start-Up Time of Deformation Localization

The spatial distribution of MS (AE) localization points can be classified into three types: cluster, discrete, and random. Spatial autocorrelation analysis can be used to quantitatively analyze the spatial distribution characteristics of MS (AE) events as they evolve over time [37]. Consequently, the spatial cluster index—*Moran's I*—is proposed as a means to track the state of deformation localization [20,38]. When the spatial distribution of MS (AE) events forms a stable cluster pattern, it indicates that the deformation localization zone is initiating. The specific calculation method is as follows:

$$Moran's\ I = \frac{n}{\sum_{i=1}^{n}\sum_{j=1}^{n} W_{ij}} \times \frac{\sum_{i=1}^{n}\sum_{j=1}^{n} W_{ij}(x_i - \overline{x})(x_j - \overline{x})}{\sum_{i=1}^{n}(x_i - \overline{x})^2} \tag{15}$$

where n is the number of region units, x_i is the observed value of the attributes of region unit i, and W_{ij} is the spatial weighting coefficient, which is equal to 1 when region i is adjacent to j and equal to 0 when region i and j are not adjacent.

If *Moran's I* is close to 1, it is a positive spatial autocorrelation with a cluster distribution; if *Moran's I* is close to -1, it is a negative spatial autocorrelation with a discrete distribution; and when *Moran's I* is equal to 0, there is no spatial autocorrelation with a random distribution.

However, due to the large volume of MS data collected at the engineering site, it is known from Equation (15) that traditional algorithms require judging the adjacency of each

spatial element. Establishing an $n \times n$ weight matrix for n elements leads to low computational efficiency and may result in the inability to obtain calculation results. Therefore, an improved version of *Moran's I* is used. The formula for the improved algorithm is as follows:

$$Moran's\ I = \frac{n}{\sum_{i=1}^{n}\sum_{j\in N(i)} W_{ij}} \times \frac{\sum_{i=1}^{n}\sum_{j\in N(i)} W_{ij}(x_i - \overline{x})(x_j - \overline{x})}{\sum_{i=1}^{n}(x_i - \overline{x})^2} \tag{16}$$

The improved method employs a face-neighborhood model within the spatial model relationship, designating elements sharing a boundary as near neighbors. That is, spatial proximity is determined based on the face-neighborhood. The calculation of W_{ij} corresponding to each pair (i, j) is performed by directly substituting into the operation without the need for storage. $N(i)$ in Equation (16) is defined as follows:

$$N(i) = \{(x_i + 1, y_i), (x_i - 1, y_i), (x_i, y_i + 1), (x_i, y_i - 1)\} \tag{17}$$

The improved algorithm segments the data into regular grids, with each grid cell potentially adjacent to a maximum of four other grid cells. Consequently, this spatial model requires only four assessments of adjacency, as illustrated in Equation (17).

3.2. Time Prediction Model

The pioneering work of Japanese scholar Saito [39] has been highly influential since the 1960 s, with its main academic ideas continuously extended and applied to predict the timing of natural geological hazards such as volcanic eruptions and earthquakes [40–42]. In this study, we propose an extended model for predicting mine earthquake occurrence times based on Saito's theory, starting with the following initial formula:

$$log_{10}^{t_r} = 2.33 - 0.916 \times log_{10}^{\dot{\varepsilon} \pm 0.59} \tag{18}$$

In Equation (18), t_r represents the predicted time of rock failure, and $\dot{\varepsilon}$ denotes the instantaneous event rate. These variables are simplified by substituting them with the time of rock failure and the instantaneous event rate during the observation period, respectively:

$$\log_{10}(t_r - t) = \log_{10} a - \log_{10} \dot{\varepsilon} \tag{19}$$

$$\dot{\varepsilon} = \frac{a}{t_r - t} \tag{20}$$

where t_r is the predicted time of rock failure, t is the observation time in real time, $\dot{\varepsilon}$ is the instantaneous event rate, and a is a constant.

Assuming that $\dot{\varepsilon} = 0$ at $t = t_0$, the following can be obtained:

$$\dot{\varepsilon} = a\log\frac{tr - t_0}{t_r - t} \tag{21}$$

which

$$\dot{\varepsilon} = \frac{\Delta d}{d_0} \tag{22}$$

Then Equation (21) can be rewritten as:

$$\Delta d = d_0 \times a \times log\frac{t_r - t_0}{t_r - t} \tag{23}$$

where Δd is the difference in relative event values between two time points and d_0 is the event value corresponding to the real-time observation time.

In practical predictions, the graphical method is employed to calculate the time of rock failure, t_r, within the observation period by integrating Equation (23). The prediction model's equation involves four unknowns: a, d_0, t_r, and t_0, which must be determined by selecting additional reference points on the cumulative event curve. To do this, three consecutive points $D_1(d_1,t_1)$, $D_2(d_2,t_2)$, and $D_3(d_3,t_3)$ are chosen from the curve, and these points must meet specific conditions:

$$d_2 - d_1 = d_3 - d_2 \tag{24}$$

By substituting the data that satisfy the conditions of Equation (24) into Equation (23), a system of three simultaneous equations is derived. This system can be simplified to yield the following relationship:

$$\frac{d_2 - d_1}{\log\frac{t_r - t_1}{t_r - t_2}} = \frac{d_3 - d_2}{\log\frac{t_r - t_2}{t_r - t_3}} \tag{25}$$

Simplify to get:

$$\frac{t_r - t_1}{t_r - t_2} = \frac{t_r - t_2}{t_r - t_3} \tag{26}$$

By moving like terms, the failure time of the rock can be obtained:

$$t_r = \frac{{t_2}^2 - t_1 t_3}{2t_2 - (t_1 + t_3)} \tag{27}$$

Equation (27) represents the time prediction model. In practical applications, it combines the graphical solution method to solve the rock failure time and sets the initiation of deformation to a fixed initial time, t_1, based on the rock's deformation evolution process. As shown in Figure 2, the graphical solution method for determining the rock failure time is schematically illustrated in the following steps:

(1) Initially, identify three consecutive points D_1, D_2, D_3, corresponding to times t_1, t_2, t_3, respectively.
(2) Select the central point D_2 and draw a vertical line towards the Y-axis. Project points D_1 and D_3 onto this vertical line, denoting the projection respectively ns as D_1' and D_3'.
(3) Determine the midpoints of D_1' and D_2 on the perpendicular line, marking it as M; similarly, find the midpoint N of D_1' and D_3 on the perpendicular line.
(4) Using D_2 as the center, draw arcs with radii MD_2 and ND_2, respectively. These arcs should intersect the perpendicular lines extending from D_2 to the X-axis at points M' and N', respectively.
(5) Extend the line connecting points D_1' and N', and find its intersection with a line parallel to the X-axis passing through point M'. From this intersection point, draw a perpendicular line to the X-axis to determine the x-coordinate, which represents t_r.

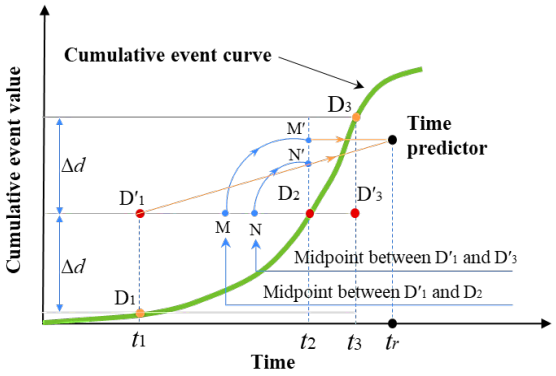


Figure 2. Graphical solution method to predict rock failure time.

The above describes the process of building the time prediction model, which mainly includes the time model prediction formula and the graphical method. Then, according to the flow chart (Figure 3), the time prediction is carried out. Figure 3 expresses the calculation process of the time prediction model: firstly, AE (MS) data are collected, and then the cumulative AE (MS) event values are calculated based on the data. A cumulative event curve (as shown in the curve diagram in Figure 2) is made, whose horizontal coordinate is time and vertical coordinate is the cumulative event value. The deformation localization start time, calculated based on the deformation localization theory, i.e., the parameter t_1. Finally, mathematical modeling software is used to calculate the unknown parameter by combining the formulas and methods in the theoretical part to get the final prediction time t_r.

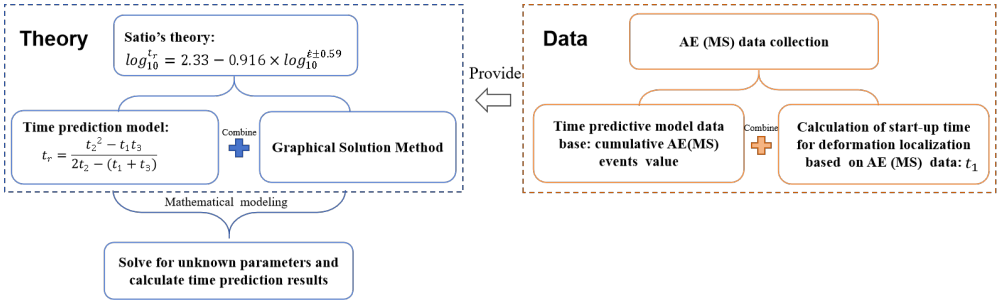


Figure 3. Flowchart of time prediction model calculation.

4. Results and Discussion

4.1. Experiments, Results and Analysis

The study mainly uses digital image correlation (DIC) technology and AE monitoring for uniaxial compression tests on red sandstone. The setup includes a loading system, a digital image capture system, and an AE system, as shown in Figure 4. Red sandstone was prepared with 50 × 50 × 100 mm cubic samples. To use DIC, the samples' surfaces were coated with black primer and white paint to make speckle patterns. For AE monitoring, three sensors were placed on both sides of the samples near the speckle area, and two on the back side, opposite the speckle field. Sensors were secured with petroleum jelly and a strong adhesive for good contact with the samples.

During the experimental preparation, the CCD camera was first precisely adjusted to ensure the clarity of the speckle pattern on the specimen surface. Meanwhile, the loading and acquisition systems were strictly synchronized to ensure data accuracy. Before commencing the experiment, initial scattering images were captured, and the acoustic emission (AE) system was initialized to minimize the background noise of the signal.

During the loading process, uniaxial compression was applied at 0.05 mm/min. The digital image system captured the specimen's surface deformation at 1 frame/s, with a resolution of 1600 × 1200 pixels, giving an object surface resolution of 0.13 mm/pixel. The AE system had a 40 dB preamplifier gain and a 10 mV threshold, operating at 3 MHz. After the experiment, data were sorted and analyzed.

Figure 5 shows the rock specimen's loading curve with six key marking points. Points 1–3 are before the peak load, point P is at the peak, and points 4 and F are post-peak, with F indicating rock failure—at half the peak stress after the peak [43,44]. Point 0 (start of loading) is the baseline for points 1-P. Post-peak points are set using the incremental method. The maximum shear strain, henceforth referred to as the deformation field, is calculated for each point, with point P as the reference for point 4, and point 4 for point F.

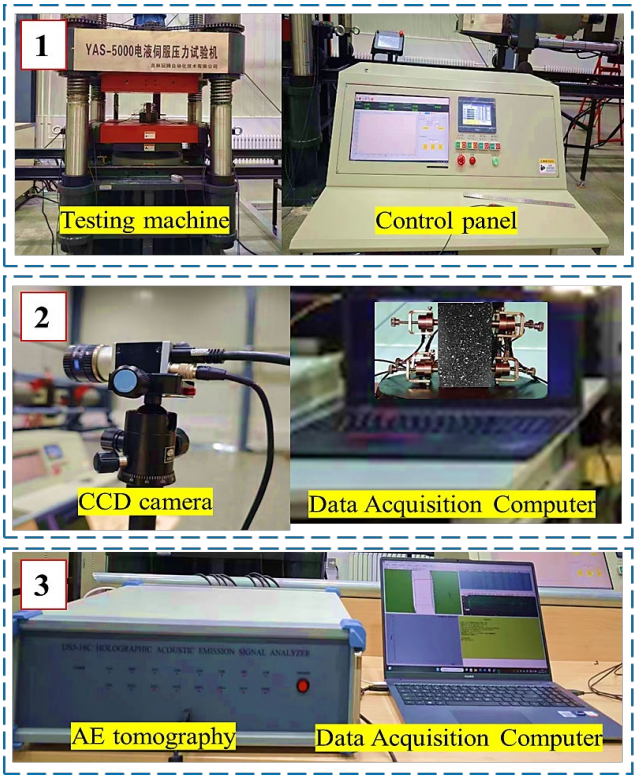


Figure 4. Diagram of the experimental system ((**1**), loading system; (**2**), digital image acquisition system; (**3**), AE acquisition system).

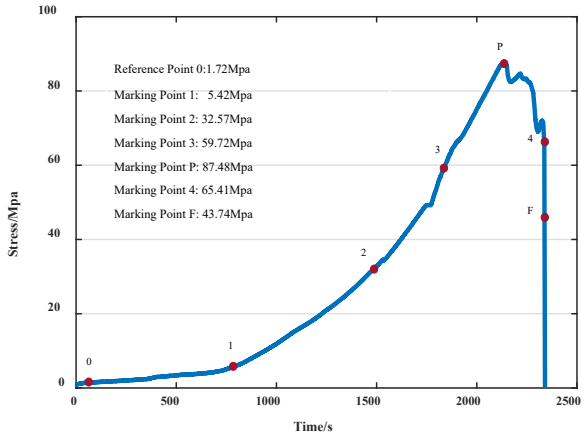


Figure 5. Specimen loading curve.

The deformation field evolution cloud map provides a clear depiction of the spatial and temporal characteristics of rock deformation damage, capturing the initiation and development of deformation localization. At marking point 1 (Figure 6 ①), the deformation field is homogeneous, coinciding with the nonlinear rise of the loading curve. By marking point 2 (Figure 6 ②), localized deformation starts in scattered areas, corresponding to the initial linear rise of the loading curve. At marking point 3 (Figure 6 ③), localized deformation concentrates at the specimen's bottom, indicating the clear start of deformation localization, during the loading curve's mid-linear rise. At the stress peak marking point *P* (Figure 6 ④), a distinct strip-shaped deformation band forms in the lower right, showing rapid development of deformation localization. At marking point 4 (Figure 6 ⑤), during the post-peak stage, the deformation band expands, with increasing strain values. Finally, at marking point *F* (Figure 6 ⑥), the deformation band evolves from single to multiple

bands, crossing the right edge, indicating the specimen has reached its stress-bearing limit and has completely failed.

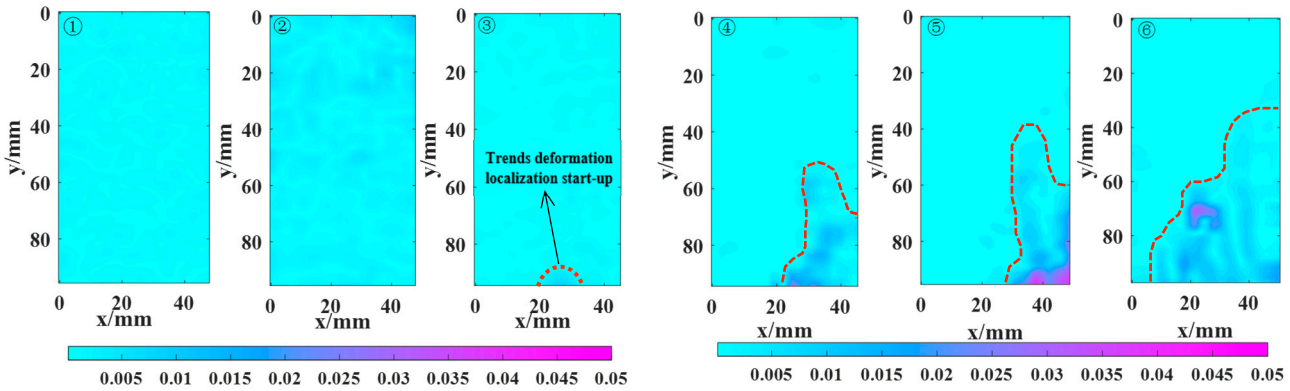


Figure 6. Deformation field evolution cloud diagram (① ② ③ ④ ⑤ ⑥ corresponds to marker points 1, 2, 3, P, 4, F, respectively).

It can be observed that the onset of deformation localization occurs during an approximately linearly increasing phase leading up to the peak load of the specimen. The ultimate failure of the rock is attributed to the continuous development of deformation localization throughout the rock mass.

4.2. Rock Failure Time Prediction Results

From the analysis of the deformation field evolution, it is determined that the initiation of deformation localization occurs approximately at the linear rise phase before the specimen reaches peak loading. The method outlined in Section 3.1 is then used to calculate the spatial aggregation index of AE events, which helps to confirm the initiation of deformation localization. Subsequently, the time prediction model, which is based on the AE cumulative event parameter, is employed to verify the reliability of the deformation localization method in predicting rock failure times.

(1) Initiation time of rock deformation localization

Based on the AE event positioning point data obtained from the aforementioned experiments, we employed the spatial cluster index calculation method to derive the index evolution curve presented in Figure 7. As observed in the figure, the index value transitions gradually from negative to positive, signifying a change in the spatial distribution pattern of the AE events from discrete to clustered. Before 1524 s, the value increases rapidly, but at 1524 s, it begins to decline. This decline indicates that a more stable spatial cluster pattern has formed, and the deformation localization zone starts to initiate. Therefore, the initiation time of deformation localization is determined to be 1524 s.

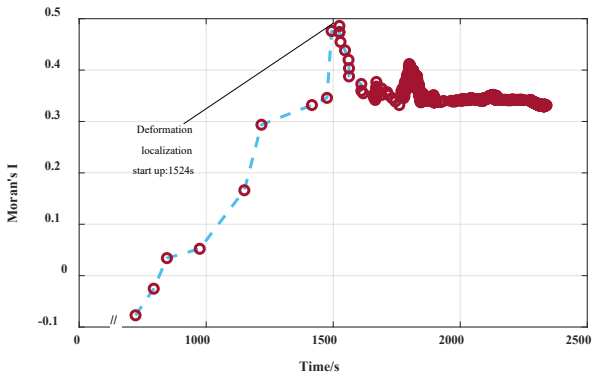


Figure 7. Deformation localization start up time for rock.

(2) Prediction Results

The precursor characteristics of the "quiet period" of AE (MS) are akin to the common phenomenon where "ringing water does not boil, and boiling water does not ring". This phenomenon is a regular manifestation of the transformation in the deformation and failure state of rock [9,45]. AE event calculations and their cumulative totals yield evolution curves (Figure 8). Initially, AE activity is low until 1850 s when it surges, then drops between 1900–2100 s, indicating the first "quiet period". AE activity peaks again, then diminishes between 2150–2250 s, marking the second "quiet period". At 2340 s, AE events spike, signaling rock failure. Thus, the "quiet period" fully reflects the state transition law of the deformation and destruction of rock. The inflection point between the two "quiet periods" is the endpoint of the advance forecast, which means it occurs after the first "quiet period" and the forecast calculation is then stopped.

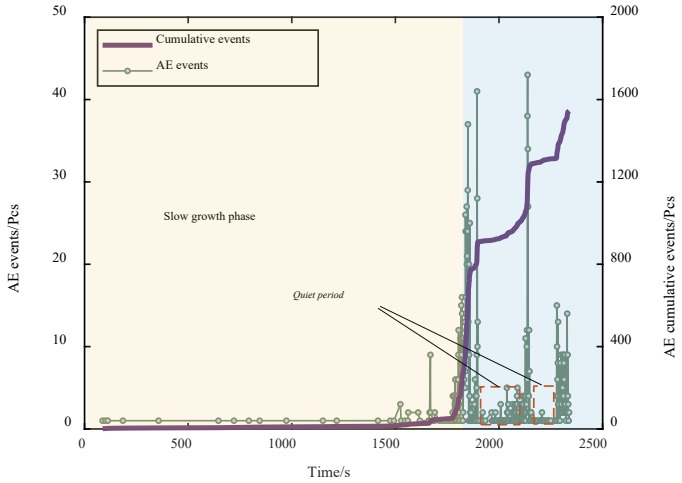
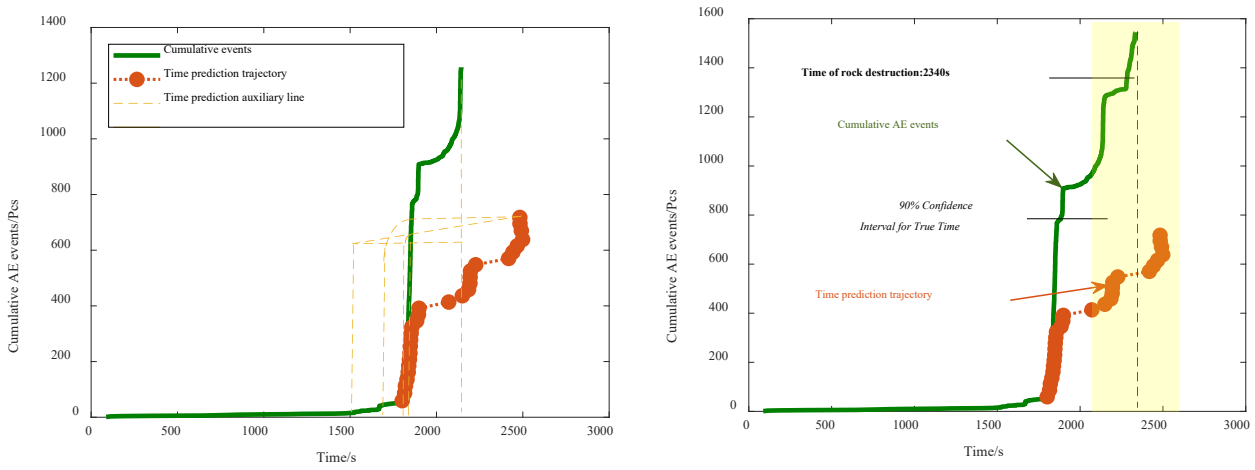


Figure 8. AE events and AE cumulative event evolution.

The AE cumulative events are selected to replace the instantaneous event rate parameter in Equation (18). Additionally, the graphical solution method is employed to predict the rock failure time. The initial time, t_1, marks the onset of deformation localization, which is at 942 s. With the initial time held constant, the final cut-off time corresponds to the end of the first "quiet period" mentioned earlier, at 2140 s. Subsequently, the failure prediction time is calculated, resulting in the modal trajectory curve for time prediction based on AE cumulative events, as depicted in Figure 9a. From the figure, it is evident that the initial phase of the prediction trajectory exhibits a monotonous upward trend, aligning with the evolutionary trend of the cumulative event curve. The predicted time increases gradually, followed by a rapid ascent until it reaches 2499 s. At this point, the time trajectory begins to fold back continuously, decreasing slowly from 2483 s until it stabilizes. The final predicted failure time ranges from 2483 s to 2499 s.

Based on the time prediction trajectory, a comparison graph between the predicted time and the actual rock failure time has been created, as shown in Figure 9b. The actual time of rock instability failure is recorded as 2340 s, while the predicted failure time falls between 2483 s and 2499 s.



(**a**) (**b**)

Figure 9. Rock failure time prediction based on cumulative AE events. (**a**) Time prediction model trajectories, (**b**) Predicted time vs. time of rock failure.

(3) Calculation of error

The prediction accuracy P is calculated by setting a 90% confidence interval for the actual failure time. If the prediction time is X, the formula for P is shown below:

$$P = \left(\frac{\sum_{i=1}^{n} I(\hat{X}_i)}{n} \right) \times 100\% \tag{28}$$

$$I(\hat{X}_i) = \begin{cases} 1, & if\ X_{lower} \le \hat{X}_i \le X_{upper} \\ 0, & if\ not \end{cases} \tag{29}$$

where X_{lower} is the lower limit of the 90% confidence interval for the actual failure time X and X_{upper} is the upper limit of the 90% confidence interval for the actual failure time X.

The earliest prediction time deviates from the actual failure time by 143 s. Considering a 90% confidence interval for the actual failure time, 100% of the predicted time points fall within this interval.

4.3. Discussion

(1) Discussion of parameters

It is evident that the prediction accuracy may correlate with the initial time t_1 and the value of the interval d. To analyze the prediction accuracy, different parameters are selected, and their influence on time prediction is examined to identify the optimal parameters.

Firstly, while keeping t_1 constant, the interval d is incrementally increased to obtain the prediction results as presented in Figure 10 and Table 1. Different values of d result in varying numbers of prediction values. The interval value has a minimal impact on prediction accuracy; however, a larger interval value tends to yield more stable prediction accuracy.

When the interval value d is consistent, various t_1 values are analyzed, and the most representative ones are selected for comparison diagrams, as illustrated in Figure 11a, which displays the comparison diagram for t_1 values that are less than the deformation localization startup time (1524 s), while Figure 11b presents the comparison diagram for t_1 values that exceed the deformation localization startup time (1524 s). Table 2 provides a more detailed breakdown of prediction accuracy values for different t_1 values. By synthesizing the information from the figures and tables, it becomes evident that when

t_1 is chosen close to the initiation of deformation localization, all predicted time points fall within the 90% confidence interval. The accuracy decreases as t_1 is selected further away from the initiation of deformation localization. When t_1 is significantly prior to the initiation of deformation localization, there is no distinct turning point, and thus, no reliable time prediction can be made.

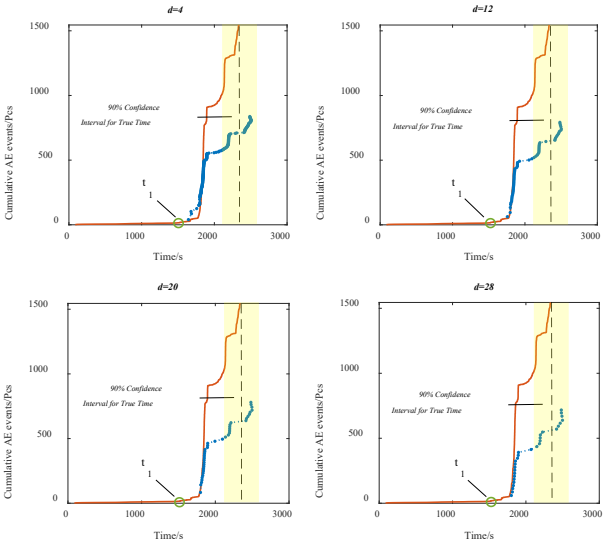
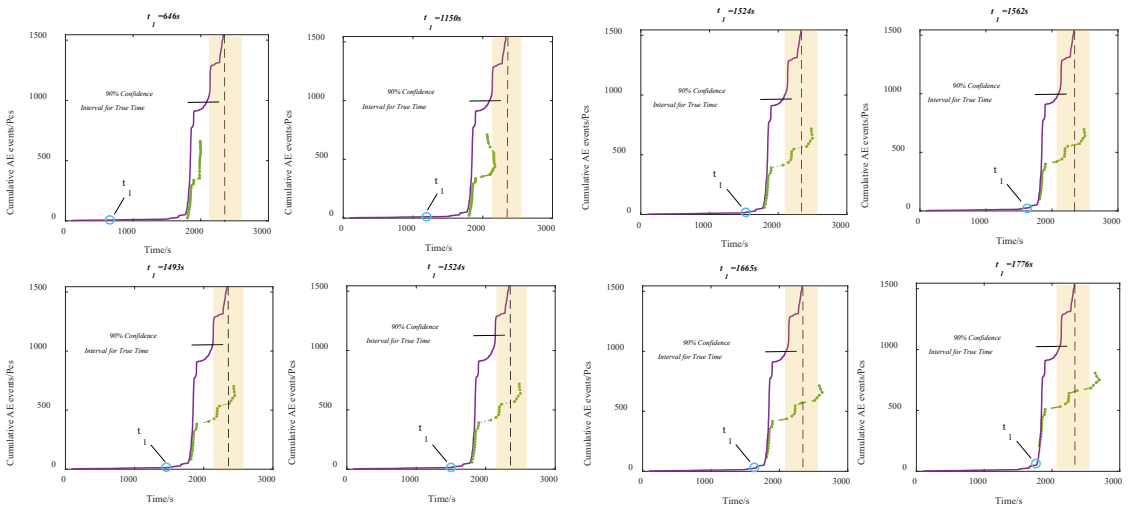


Figure 10. Predicted time vs. actual damage time when t_1 is the same and d is different.

Table 1. Prediction accuracy when t_1 is the same and d is different.

No.	t_1/s	*d*/*Pcs*	Predicted Time Range/s	Predictive Accuracy at 90% Confidence Intervals/%
1	1524	4	2491~2509	100
2	1524	8	2483~2506	100
3	1524	12	2483~2502	100
4	1524	16	2483~2499	100
5	1524	20	2483~2502	100
6	1524	24	2483~2499	100
7	1524	28	2483~2499	100
8	1524	32	2483~2499	100



(**a**) (**b**)

Figure 11. Predicted time vs. actual damage time when d is the same and t_1 is different. (**a**) $t_1 \leq 1524$ s, (**b**) $t_1 \geq 1524$ s.

Table 2. Prediction accuracy when d is the same and t_1 is different.

No.	*d*/*Pcs*	t_1/s	Predicted Time Range/s	Predictive Accuracy at 90% Confidence Intervals/%
1	28	646	/	0
2	28	721	/	0
3	28	793	/	0
4	28	845	2061~2076	0
5	28	974	2017~2108	20
6	28	1150	2063~2174	67
7	28	1217	2089~2203	73
8	28	1416	2168~2234	100
9	28	1475	2232~2253	100
11	28	1493	2433~2449	100
12	28	1524	2483~2499	100
13	28	1562	2485~2501	100
14	28	1610	2519~2543	100
15	28	1665	2583~2626	0
16	28	1712	2627~2660	0
17	28	1776	2638~2700	0
18	28	1800	2861~2752	0

/: No inflection point has occurred.

(2) Applicability

The optimal parameters were further introduced into different rock specimens for prediction and the predicted results were obtained as shown in Table 3, where the first column is the rock number, the second column is the peak stress of the rock, the third column is the actual time of failure, the fourth column is the predicted time range, and the fifth column is the prediction accuracy. From the accuracy of prediction shown in the table, it can be seen that in other groups of rocks, the method also obtained better prediction results, thus proving the applicability of the method.

Table 3. Predicted results for different rock specimens.

No.	Peak Stress/Mpa	Actual Time of Failure/s	Predicted Time Range/s	Predictive Accuracy at 90% Confidence Intervals/%
1-1	87.48	2340	2483~2499	100
1-2	86.11	2300	2455~2522	100
1-3	79.24	2253	2444~2468	100
1-4	82.41	2278	2460~2480	100
1-5	77.75	2230	2316~2451	100
1-6	74.30	2225	2420~2440	100

(3) Limitations

Although the method is capable of quantitatively describing the initiation time of deformation localization, from the discussion of the parameters in Table 2, it can be seen that when the deformation localization initiation time is set as t_1, all the prediction points fall within the confidence interval. In addition, even when the proximity to the deformation localization initiation moment is chosen as t_1, the prediction points also lie within the confidence interval. However, there are differences in their prediction time ranges. It would be time-consuming and inefficient to manually determine the optimal t_1. Therefore, this study anticipates incorporating machine learning techniques for parameter optimization in the future, with a view to obtaining higher prediction accuracy.

5. Application in Coal Mines

5.1. Overview of Working Face

The $3^{-1}105$ working face, located in a mine in Inner Mongolia, is situated in the central part of the 3–11 mining area. It spans a strike length of 2671.5 m, with a working face length varying between 280 and 291 m, resulting in an area of 766,492 m^2. The tectonic form of the working face is characterized by a monoclinic structure that generally dips to the west, with a dipping angle ranging from 1~7°. The stratigraphic yield exhibits some variation along the strike and dip, but these changes are not significant.

The working face intersects the NF40 fault, ranging from 0 to 3 m in throw, and the NF37 and NF39 faults, which may be encountered during mining. Mining started in October 2020, with MS monitoring technology in use throughout. The blue solid circle in Figure 12 marks the probe's movement with the working face.

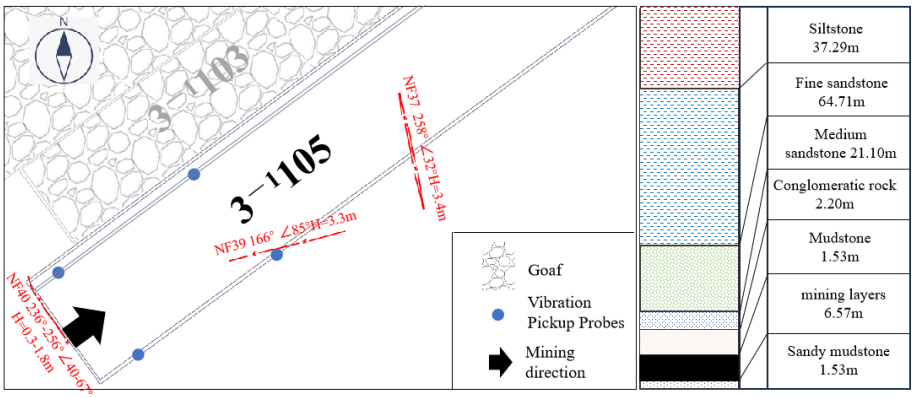


Figure 12. Schematic diagram of the working face and geological boreholes.

The direct roof of the coal seam consists of sandy mudstone and fine sandstone, moderately fractured with developed laminations and a blocky structure. The main roof is light grey, medium-coarse-grained sandstone, mainly composed of quartz and feldspar, sub-angular, moderately sorted, and semi-hard with muddy cementation. The coal seam floor is grey-black sandy mudstone with horizontal laminations and flat or shell-like fractures, interbedded with carbonaceous mudstone and thin coal seams, showing cementation. Geological borehole histograms are shown in Figure 12.

5.2. Forecasting the Time Frame of Mine Earthquakes

MS data from the working face, gathered from 1 November 2020 to 2 April 2021, was analyzed. A major mine earthquake hit the working face on 2 April, which was accompanied by an MS event of 2.13×10^6 J energy. Figure 13 shows the MS energy trend. Before 18 February, MS event energies were low, peaking at 10^4 J. On 18 February, an 8.21×10^4 J event occurred, after which energy dropped until another high-energy event on 2 April. The cumulative energy curve rose slowly until 18 February, when it stepped up and then continued to grow until 2 April's sudden increase. This indicates energy built up in the rock mass before the earthquake, with the 18 February release not being enough to discharge it fully.

Figure 14 displays the daily and cumulative frequency of MS events. With the energy evolution curves, it is observed that MS events peaked at 3800 on 22 March, with a trend surge, contrasting with the "quiet period" before 1 April's mine earthquake, marked by reduced MS activity. This quiet period precedes the inflection point in the MS cumulative frequency curve, signaling the mine earthquake's imminent occurrence.

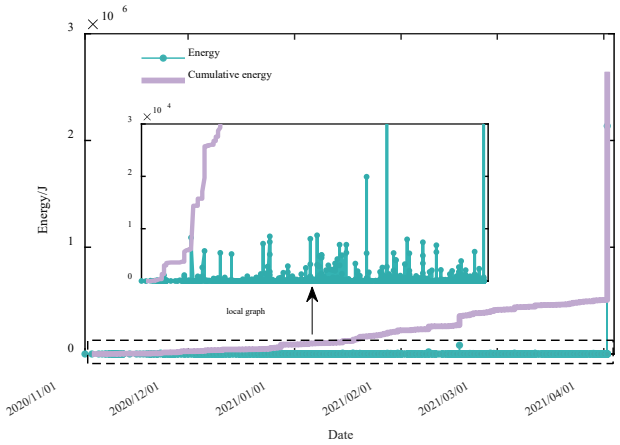


Figure 13. MS energy evolution curve.

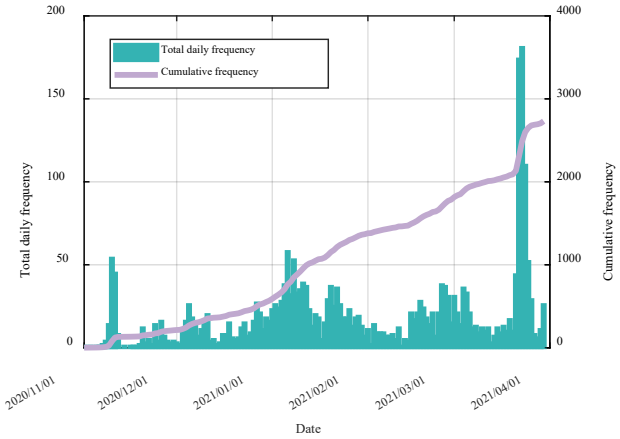


Figure 14. MS event evolution curve.

To further analyze the initiation time of deformation localization of MS events, Figure 15 presents the index evolution curve. It is observable from this curve that the index increases rapidly in the early stage, transitioning from negative to positive values, until it peaks on the 38th day of the monitoring period. Following this peak, the value begins to decline, suggesting that a stable spatial clustering pattern for MS events has been established by the 38th day.

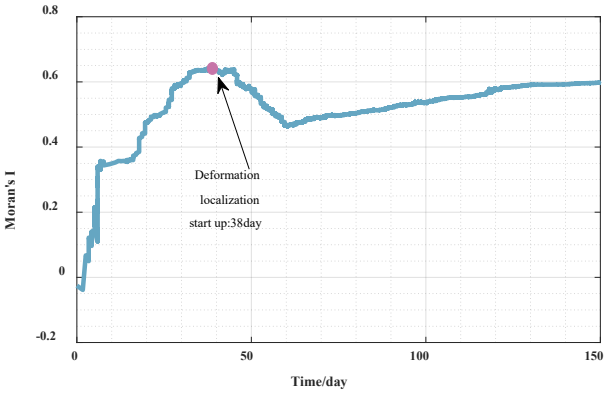
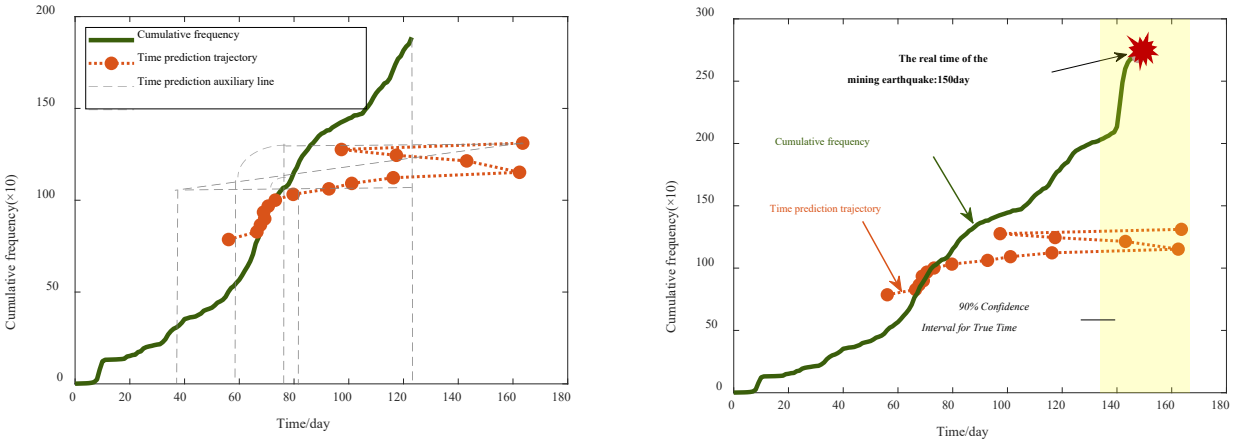


Figure 15. Deformation localization start up time.

Using the rock failure time prediction method described earlier, the cumulative frequency of MS events replaces the instantaneous event rate parameter in Equation (19). By integrating the graphical solution method, the occurrence time of mine earthquakes is

predicted. The initial time t_1 is maintained as the start of deformation localization, which is 38 days. With the initial time held constant and the final cut-off time set to 123 days, the time prediction model trajectory curve based on the cumulative frequency of MS events is derived, as illustrated in Figure 16a. The initial stage of the prediction trajectory in Figure 16a exhibits a steady upward trend, closely aligning with the evolutionary trend of the cumulative frequency curve. The prediction time increases gradually, followed by a significant rise in the predicted time volume until the 162nd day. Subsequently, the predicted time trajectory begins to fold back, reaching the 97th day, and then continues to fall back to the 163rd day. The final predicted damage time is estimated to be between the 97th and 163rd days.



(**a**) (**b**)

Figure 16. Predicted timing of mine earthquakes. (**a**) Time prediction model trajectories, (**b**) Predicted timing vs. the timing of mine earthquakes.

Furthermore, according to the time prediction trajectory, a plot of the predicted mine earthquake times against the actual occurrence times has been generated, as depicted in Figure 16b. From this plot, it is observed that the actual mine earthquake occurred on the 150th day, whereas the predicted time frame for the event spans from the 98th to the 163rd day. The earliest predicted time deviates from the actual occurrence time by 34.6%. A 90% confidence interval has been calculated for the actual time of the mine earthquake, and it is found that 60% of the predicted time points fall within this interval. Notably, the last prediction point lies precisely within the 90% confidence interval.

6. Conclusions

The study introduces a method for predicting the timing of mine earthquakes using rock deformation localization. It establishes a theoretical link between mine earthquakes and rock deformation localization and develops a time prediction model based on Saito's theory. This model has demonstrated accuracy in predicting both rock failure times and the occurrence times of mine earthquakes.

(1) Deformation localization and the "quiet period" of MS(AE) are identified as two key precursory characteristics. The model uses the initiation time of deformation localization and the inflection point of the "quiet period" of MS(AE) activity as primary parameters.

(2) For predicting rock failure times, the earliest prediction time deviates from the actual failure time by 143 s. The accuracy rate of predicted time points falling within a 90% confidence interval of the actual failure times is 100%

(3) The prediction accuracy is observed to improve as the starting time parameter more closely approximates the actual initiation time of deformation localization.
(4) In this study, the model predicted the time of mine earthquakes through the state of rock deformation, addressing the limitations of traditional theoretical models that could not quantify such events and reducing the over-reliance on indicators seen in statistical and machine learning models. The model's accuracy in predicting the time of mine earthquakes is 60%, indicating room for improvement and limitations of the method. The predictive ability of the model can be enhanced by further adopting machine learning techniques for parameter optimization and refining and calibrating the model with additional data.

Author Contributions: Conceptualization, methodology, data curation, writing—original draft preparation, C.Z.; supervision, methodology, writing—review and editing, L.D.; supervision, methodology, writing—review and editing, Y.S.; data curation, Y.L. All authors have read and agreed to the published version of the manuscript.

Funding: This research was funded by National Key Research and Development Program grant number 2022YFC3004603, Youth Talent Support Program of 'Xing Liao Talent Program' grant number XLYC2203003, National Natural Science Foundation of China grant number 62072220, Natural Science Foundation of Liaoning Province grant number 2022-KF-13-06.

Data Availability Statement: The datasets used and analyzed in the current study are available from the corresponding author on reasonable request.

Conflicts of Interest: The authors declare no conflicts of interest.

References

1. Li, T.; Cai, M.F.; Cai, M. A review of mining-induced seismicity in China. *Int. J. Rock Mech. Min. Sci.* **2007**, *44*, 1149–1171. [CrossRef]
2. Pan, Y.S.; Song, Y.M.; Liu, J. Pattern, change and new situation of coal mine rockburst prevention and control in China. *Chin. J. Rock Mech. Eng.* **2023**, *42*, 2081–2095.
3. Hooshangi, H.; Hadianfard, M.A.; Dehghan, S.M.; Johari, A. Stochastic selection of earthquake records in structural probabilistic analyses. *J. Constr. Steel Res.* **2024**, *219*, 108803. [CrossRef]
4. Hooshangi, H.; Hadianfard, M.A.; Johari, A. The reliability assessment of the seismic demands of beams in chevron-braced frames and the factors affecting them. *Structures* **2024**, *66*, 106876. [CrossRef]
5. Cao, A.Y.; Dou, L.M.; Bai, X.X.; Liu, Y.Q.; Yang, K.; Li, J.Z.; Wang, C.B. State-of-the-art occurrence mechanism and hazard control of mining tremors and their challenges in Chinese coal mines. *J. China Coal Soc.* **2023**, *48*, 1894–1918.
6. Zhu, J.B.; Ma, B.W.; Xie, H.P.; Gao, F.; Zhou, H.W.; Zhou, C.T.; Zhen, F.R. Differences and connections between mining seismicity and coal bursts in coal mines and preliminary study on coal bursts induced by mining seismicity. *J. China Coal Soc.* **2022**, *47*, 3396–3409.
7. Li, H.L.; Bai, Y.L.; Xia, M.F.; Ke, F.J.; Yin, X.C. Damage localization as a possible precursor of earthquake rupture. *Pure Appl. Geophys.* **2000**, *157*, 1929–1943. [CrossRef]
8. Pan, Y.S.; Yang, X.B.; Ma, S.P.; Xu, B.J. Experimental study on the deformation localization of rock-soil material. *J. China Coal Soc.* **2002**, *27*, 281–284.
9. Song, Y.M.; Xing, T.Z.; Zhao, T.B.; Zhao, Z.X.; Gao, P.B. Acoustic emission characteristics of deformation field development of rock under uniaxial loading. *Chin. J. Rock Mech. Eng.* **2017**, *36*, 534–542.
10. Song, Y.M.; Jiang, Y.D.; Ma, S.P.; Yang, X.B.; Zhao, T.B. Evolution of deformation fields and energy in whole process of rock failure. *Rock Soil. Mech.* **2012**, *33*, 1352–1356.
11. Hao, S.W.; Wang, H.Y.; Xia, M.F.; Bai, Y.L. Relationship between strain localization and catastrophic rupture. *Theor. Appl. Fract. Mech.* **2007**, *48*, 41–49. [CrossRef]
12. Hao, S.W.; Xia, M.F.; Ke, F.J.; Bai, Y.L. Evolution of localized damage zone in heterogeneous media. *Int. J. Damage Mech.* **2010**, *19*, 787–804. [CrossRef]
13. Xue, J.; Hao, S.; Wang, P.; Yang, R.; Bai, Y. Localization of deformation and its effects on power-law singularity preceding catastrophic rupture in rocks. *Int. J. Damage Mech.* **2020**, *29*, 86–102. [CrossRef]

14. Li, D.; Zhang, J.F.; Wang, C.W.; Jiang, F.X. Propagation patterns of microseismic waves in rock strata during mining: An experimental study. *Int. J. Miner. Metall. Mater.* **2019**, *26*, 531–537. [CrossRef]
15. Liu, J.P.; Wang, R.; Lei, G.; Ying, T.S.; Shi, D.X.; Yuan, H.L. Studies of stress and displacement distribution and the evolution law during rock failure process based on acoustic emission and microseismic monitoring. *Int. J. Rock Mech. Min. Sci.* **2020**, *132*, 104384. [CrossRef]
16. Wang, J.X.; Tang, S.B.; Heap, M.J.; Tang, C.A.; Tang, L.X. An auto-detection network to provide an automated real-time early warning of rock engineering hazards using microseismic monitoring. *Int. J. Rock Mech. Min. Sci.* **2021**, *140*, 104685. [CrossRef]
17. He, X.Q.; Zhou, C.; Song, D.Z.; Li, Z.L.; Gao, A.Y.; He, S.Q.; Khan, M. Mechanism and monitoring and early warning technology for rockburst in coal mines. *Int. J. Miner. Metall. Mater.* **2021**, *28*, 1097–1111. [CrossRef]
18. Wang, K.K.; Ma, K.; Tang, C.A.; Liu, H.Y.; Wang, X.T.; Li, Q. Study on deep mining-induced strata behavior based on the evolutional laws of multiple indices from microseismic monitoring. *Rock Mech. Rock Eng.* **2023**, *56*, 6481–6501. [CrossRef]
19. Feng, L.F.; Wang, H.; Wang, X.D.; Zhang, Q. Microfracture evolution characteristics and precursor identification of coal impact failure. *Chin. J. Rock Mech. Eng.* **2022**, *41*, 1440–1452.
20. Pan, Y.S.; Song, Y.M.; Zhu, C.L.; Ren, H.; Xu, H.L. Localization method of coal rock deformation for rock burst prediction. *J. China Coal Soc.* **2023**, *48*, 185–198.
21. Jia, H.W.; Yan, B.X.; Yang, Z.; Yilmaz, E. Identification of goaf instability under blasting disturbance using microseismic monitoring technology. *Geomech. Geophys. Geo-Energy Geo-Resour.* **2023**, *9*, 142. [CrossRef]
22. Wang, A.W.; Li, C.; Pan, Y.S.; Song, Y.M.; Fan, D.W.; Wei, C.Q.; Yu, X.H.; Lu, C. Dynamic identification method for rockburst hazard areas based on multivariate geophysical indicators and its application. *J. China Coal Soc.* **2024**, *49*, 2573–2588.
23. Lai, X.P.; Xu, H.C.; Shan, P.F.; Hu, Q.X.; Ding, W.X.; Yang, S.T.; Yan, Z.M. Research on the mechanism of rockburst induced by mined coal-rock linkage of sharply inclined coal seams. *Int. J. Miner. Metall. Mater.* **2024**, *31*, 929–942. [CrossRef]
24. Xu, C.; Si, J.J.; Guan, Z.Y.; Zhao, W.; Wu, Y.; Gao, X.Y. Reliable conflictive multi-view learning. *AAAI Conf. Artif. Intell.* **2024**, *38*, 16129–16137. [CrossRef]
25. Liu, Y.; Xu, C.; Chen, L.; Yan, M.; Zhao, W.; Guan, Z.Y. TABLE: Time-aware Balanced Multi-view Learning for stock ranking. *Knowl.-Based Syst.* **2024**, *303*, 112424. [CrossRef]
26. Zhao, W.; Xu, C.; Guan, Z.Y.; Wu, X.L.; Zhao, W.Q.; Miao, Q.G.; He, X.F.; Wang, Q. TelecomNet: Tag-Based Weakly-Supervised Modally Cooperative Hashing Network for Image Retrieval. *IEEE Trans. Pattern Anal. Mach. Intell.* **2022**, *11*, 7940–7954. [CrossRef]
27. Liu, C.L.; Wu, Z.H.; Wen, J.; Xu, Y.; Huang, C. Localized sparse incomplete multi-view clustering. *IEEE Trans. Multimed.* **2023**, *25*, 5539–5551. [CrossRef]
28. Wen, J.; Liu, C.L.; Deng, S.J.; Liu, Y.C.; Fei, L.K.; Yan, K. Deep double incomplete multi-view multi-label learning with incomplete labels and missing views. *IEEE Trans. Neural Netw. Learn. Syst.* **2024**, *8*, 11396–11408. [CrossRef]
29. Liu, C.L.; Wen, J.; Wu, Z.H.; Luo, X.L.; Huang, C.; Xu, Y. Information recovery-driven deep incomplete multiview clustering network. *IEEE Trans. Neural Netw. Learn. Syst.* **2024**, *11*, 15442–15452. [CrossRef] [PubMed]
30. Guo, Y.J.; Lei, X.J.; Liu, L.; Pan, Y. circ2CBA: Prediction of circRNA-RBP binding sites combining deep learning and attention mechanism. *Front. Comput. Sci.* **2023**, *17*, 175904. [CrossRef]
31. Zhao, L.L.; Song, S.T.; Wang, P.Y.; Wang, P.Y.; Wang, J.J.; Guo, M.Z. A MLP-Mixer and mixture of expert model for remaining useful life prediction of lithium-ion batteries. *Front. Comput. Sci.* **2024**, *18*, 185329. [CrossRef]
32. Ma, L.; Cai, J.J.; Dai, X.G.; Jia, R.H. Research on Rockburst Risk Level Prediction Method Based on LightGBM−TCN−RF. *Appl. Sci.* **2022**, *12*, 8226. [CrossRef]
33. Ma, K.; Shen, Q.Q.; Sun, X.Y.; Ma, T.H.; Hu, J.; Tang, C.A. Rockburst prediction model using machine learning based on microseismic parameters of Qinling water conveyance tunnel. *J. Cent. South Univ.* **2023**, *30*, 289–305. [CrossRef]
34. Basnet, P.M.S.; Jin, A.B.; Mahtab, S. Applying machine learning approach in predicting short-term rockburst risks using microseismic information: A comparison of parametric and non-parametric models. *Nat. Hazards* **2024**, 1–28. [CrossRef]
35. Sun, J.H.; Wang, W.J.; Xie, L.K. Predicting short-term rockburst intensity using a weighted probability stacking model with optimal feature selection and Bayesian hidden layer. *Tunn. Undergr. Space Technol.* **2024**, *153*, 106021. [CrossRef]
36. Pan, Y.S.; Zhao, Y.F.; Ma, J. Discussion on rockburst influenced by regional stress field in China. *Chin. J. Rock Mech. Eng.* **2005**, *24*, 2847–2853.
37. Chu, C.Q.; Wu, S.C.; Zhang, C.J.; Zhang, Y.L. Microscopic damage evolution of anisotropic rocks under indirect tensile conditions: Insights from acoustic emission and digital image correlation techniques. *Int. J. Miner. Metall. Mater.* **2023**, *30*, 1680–1691. [CrossRef]
38. Wang, S.Y.; Si, G.Y.; Wang, C.B.; Cai, W.; Li, B.L.; Joung, O.; Canbulat, I. Quantitative assessment of the spatio-temporal correlations of seismic events induced by longwall coal mining. *J. Rock Mech. Geotech. Eng.* **2022**, *14*, 1406–1420. [CrossRef]
39. Saito, M. Forecasting time of slope failure by tertiary creep. In Proceedings of the 7th International Conference on Soil Mechanics and Foundation Engineering, Mexico City, Mexico, 25–29 August 1969; pp. 677–683.
40. Voight, B. A relation to describe rate-dependent material failure. *Science* **1989**, *243*, 200–203. [CrossRef] [PubMed]

41. Main, I.G. Applicability of time-to-failure analysis to accelerated strain before earthquakes and volcanic eruptions. *Geophys. J. Int.* **1999**, *139*, F1–F6. [CrossRef]
42. Main, I.G. Prediction of failure times in the Earth for a time-varying stress. *Geophys. J. Int.* **1988**, *92*, 455–464.
43. Zhao, Y.S. Retrospection on the development of rock mass mechanics and the summary of some unsolved centennial problems. *Chin. J. Rock Mech. Eng.* **2021**, *40*, 1297–1336.
44. Feng, Z.C.; Lv, Z.X.; Zhao, Y.S. Research progress on short-impending prediction of rock failure—Comments on the competition of short-impending prediction of rock failure. *Chin. J. Rock Mech. Eng.* **2022**, *41*, 2522–2529.
45. Li, Z.L.; He, S.Q.; Song, D.Z.; Sun, Y.X.; Li, J.J.; Wang, X.Y. Microseismic temporal-spatial precursory characteristics and early warning method of rockburst in steeply inclined and extremely thick coal seam. *Energies* **2021**, *14*, 1186. [CrossRef]

Disclaimer/Publisher's Note: The statements, opinions and data contained in all publications are solely those of the individual author(s) and contributor(s) and not of MDPI and/or the editor(s). MDPI and/or the editor(s) disclaim responsibility for any injury to people or property resulting from any ideas, methods, instructions or products referred to in the content.